CHEMISTRY OF MATERIALS

ARTICLE

pubs.acs.org/cm

Displacive Phase Transitions and Magnetic Structures in Nd-Substituted $BiFeO_3$

I. Levin,*[,†] M. G. Tucker,[‡] H. Wu,[†] V. Provenzano,[†] C. L. Dennis,[†] S. Karimi,[§] T. Comyn,[∥] T. Stevenson,[∥] R. I. Smith,[‡] and I. M. Reaney[§]

[†]National Institute of Standards and Technology, Gaithersburg, Maryland 20899, United States

[‡]ISIS Facility, Rutherford Appleton Laboratory, Didcot OX11 0QX, United Kingdom

[§]Department of Engineering Materials, University of Sheffield, Sheffield, S1 3JD, United Kingdom

[∥]Institute for Materials Research, University of Leeds, LS2 9JT, United Kingdom

ABSTRACT: Neutron powder diffraction was used to determine changes in the nuclear and magnetic structures of $Bi_{1-x}Nd_xFeO_3$ polymorphs involved in the first-order displacive phase transitions from the high-temperature nonpolar phase to the low temperature polar ($x \leq 0.125$) and antipolar ($0.125 \leq x \leq 0.25$) phases, respectively. The high-temperature phase (O_1), which crystallizes with a structure similar to the room-temperature form of $NdFeO_3$, exhibits *Pbnm* symmetry and unit cell $\sqrt{2}a_c \times \sqrt{2}a_c \times 2a_c$ (where $a_c \approx 4$ Å is the lattice parameter of an ideal cubic perovskite), determined by $a^-a^-c^+$ octahedral tilting. The low-temperature polar structure (R) is similar to the β-phase of $BiFeO_3$ and features rhombohedral symmetry determined by $a^-a^-a^-$ octahedral rotations and cation displacements. The recently discovered antipolar phase (O_2) resembles the antiferroelectric *Pbam* ($\sqrt{2}a_c \times 2\sqrt{2}a_c \times 2a_c$) structure of $PbZrO_3$ but with additional displacements that double the $PbZrO_3$ unit cell along the *c*-axis to $\sqrt{2}a_c \times 2\sqrt{2}a_c \times 4a_c$ and yield *Pbnm* symmetry. The $O_1 \leftrightarrow R$ and $O_1 \leftrightarrow O_2$ transitions are both accompanied by a large discontinuous *expansion* of the lattice volume in the low-temperature structures with a contrasting contraction of the [FeO_6] octahedral volume and an abrupt decrease in the magnitude of octahedral rotations. The $O_1 \leftrightarrow O_2$ transition, which occurs in the magnetic state, is accompanied by an abrupt ≈90° reorientation of the magnetic dipoles. This coupling between the nuclear and magnetic structures is manifested in a significant magnetization anomaly. Below 50 K, reverse rotation of magnetic dipoles back to the original orientations in the high-temperature O_1 structure is observed.

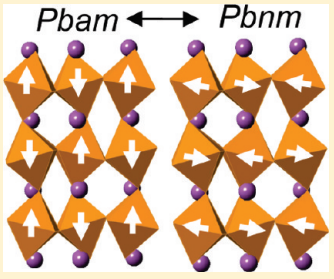

KEYWORDS: perovskites, multiferroics, phase transitions, ferroelectrics, magnetic ordering, bismuth ferrite

INTRODUCTION

Perovskite-like $BiFeO_3$ exhibits ferroelectric and magnetic properties which are of interest for several electronic applications.[1,2] At room temperature, $BiFeO_3$ crystallizes with rhombohedral *R*3*c* symmetry in which $a^-a^-a^-$ rotations[3] of oxygen octahedra are combined with polar cation displacements along the threefold axis.[4,5] At ≈1100 K, the rhombohedral (R) phase undergoes a first order phase transition to a $GdFeO_3$-like paraelectric structure (O_1) featuring $a^-a^-c^+$ octahedral tilting and *Pbnm* (No. 62) symmetry (lattice parameters $\sqrt{2}a_c \times \sqrt{2}a_c \times 2a_c$, where a_c (≈4 Å) is the lattice parameter of an ideal cubic perovskite).[6] The $R \leftrightarrow O_1$ transition is accompanied by a large discontinuous lattice-volume contraction in the high-temperature O_1 phase.[6] In addition to structural distortions, $BiFeO_3$ exhibits G-type antiferromagnetic (AFM) ordering (Neel temperature 650 K) with a long-wavelength spiral modulation of magnetic spins which reportedly precludes development of a net magnetization in this material.[7]

Partial substitution of Bi by rare-earth (RE) ions is known to induce a ferromagnetic response which has been attributed to suppression of the spiral modulation.[8−10] The temperature of the ferroelectric to paraelectric phase transition decreases rapidly with increasing rare-earth substitution[11] (Figure 1). Recent studies of bulk and thin film (Bi,RE)FeO_3 (RE = Nd, Sm) revealed formation of a stable antipolar, $PbZrO_3$-like structure (O_2) in a narrow rare-earth concentration range.[11−14] The stability domain for this phase is considerably larger for Nd substitution compared to Sm.[11] On heating, the O_2 structure transforms to O_1 (Figure 1) via a first order phase transition which is accompanied by a large discontinuous volume decrease, similar to the $R \leftrightarrow O_1$ transition in $BiFeO_3$.[15] The $O_2 \leftrightarrow O_1$ transition occurs in the AFM state (Figure 1) and is accompanied by abrupt 90° reorientation of magnetic dipoles within the same AFM-ordered array, which is also manifested in a pronounced change in magnetization.[15] Despite average AFM ordering, the O_2 phase exhibits a robust ferromagnetic response,[15] possibly caused by canting of magnetic moments. Similarities between the O_2 and antiferroelectric $PbZrO_3$ structures suggested an antiferroelectric nature for the O_2 phase, thus raising an intriguing prospect of an antiferroelectric antiferromagnet/ferromagnet.

The $R \leftrightarrow O_1$ transition in $BiFeO_3$ has been analyzed by Arnold et al.[6] using neutron diffraction; however, some important structural effects, such as changes in octahedral volumes or tilting angles across the transition, remained unclear. In the present

Received: December 29, 2010
Revised: February 18, 2011
Published: March 22, 2011

study, we applied variable-temperature neutron diffraction combined with transmission electron microscopy to compare structural changes that occur at the $R \leftrightarrow O_1$ and $O_2 \leftrightarrow O_1$ transitions in (Bi,Nd)FeO_3. The lower transition temperatures in the Nd-substituted $BiFeO_3$ compared to pure $BiFeO_3$ facilitate measurements of the high-temperature phase because $BiFeO_3$ starts to decompose at temperatures near the $R \leftrightarrow O_1$ transition. Neutron diffraction along with variable-temperature magnetic measurements were also used to determine changes in the magnetic structure. This contribution extends our previous brief report[15] on the coupling between the $O_2 \leftrightarrow O_1$ transition and the magnetic structure in $Bi_{1-x}Nd_xFeO_3$. Here, we show that the $R \leftrightarrow O_1$ and $O_2 \leftrightarrow O_1$ transitions exhibit strong similarities despite their different atomic displacements/distortions. For example, in both cases, the $[FeO_6]$ octahedral volume contracts with a corresponding decrease in the magnitude of the octahedral rotations below the transition, in sharp contrast to an abrupt expansion of the unit cell volume. The magnetic moments that switch by 90° at the $O_1 \rightarrow O_2$ transition undergo a reverse transition toward their original orientations in the high-temperature phase upon further cooling below 50 K.

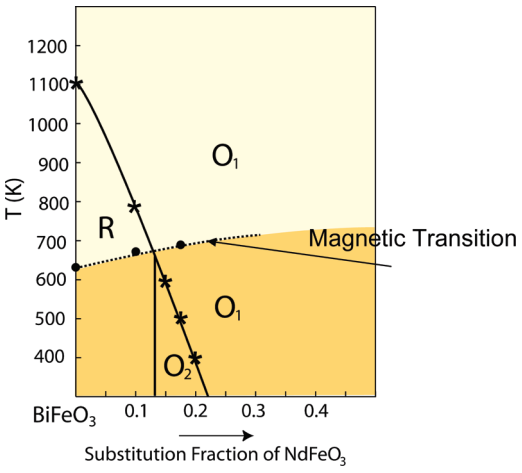

Figure 1. Schematic T_0 diagram indicating structural and magnetic transitions in the $BiFeO_3$-rich part of the (Bi,Nd)FeO_3 system. The temperatures of the structural phase transitions were deduced from variable-temperature neutron diffraction measurements, whereas the temperatures of the magnetic transitions were inferred from magnetic measurements. The O_1 phase is paraelectric, R phase is ferroelectric, and O_2 phase is supposedly antiferroelectric.

EXPERIMENTAL SECTION

$Bi_{1-x}Nd_xFeO_3$ samples (x = 0.1, 0.15, 0.175, 0.2) were prepared by conventional solid state synthesis. Bi_2O_3 (99.999%), Nd_2O_3 (99.999%, predried at 700 °C), and Fe_2O_3 (A.G.) powders were mixed by grinding under acetone with an agate mortar and pestle, dried, pressed into pellets, and heat treated in air at 850 °C for 5 h. The samples were subjected to multiple heat treatments (with intermediate grindings) at 920 °C for a total time of 200 h until no detectable changes in the width of X-ray reflections could be observed. Thermogravimetric analyses indicated no detectable weight loss under these heat-treatment conditions. As reported previously,[15] the large volume change, which accompanies

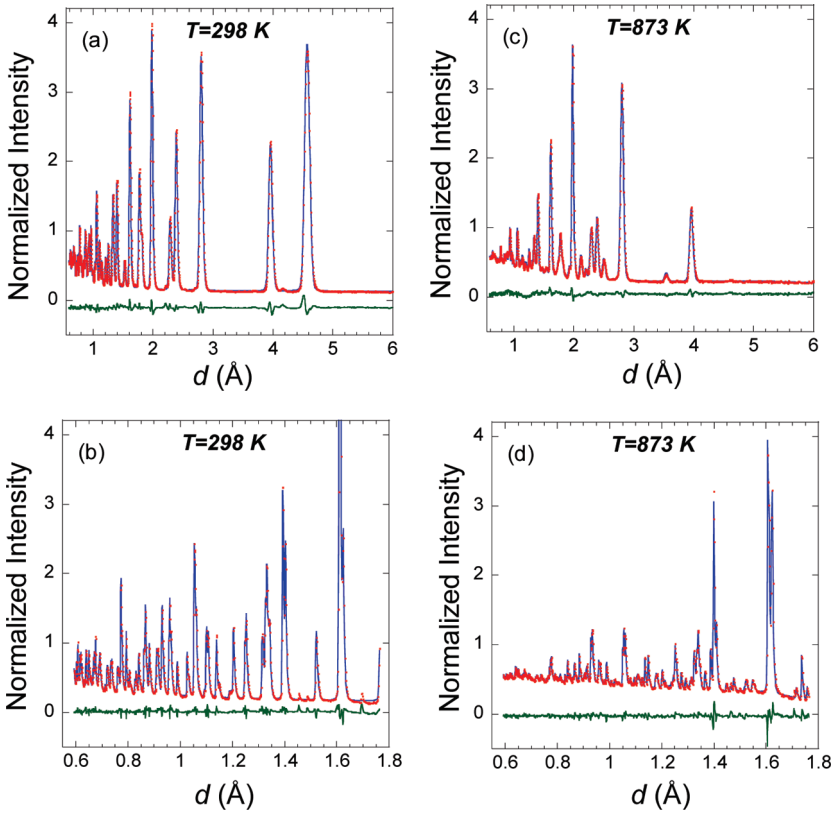

Figure 2. (a, b) Experimental (crosses) and calculated (line) neutron powder diffraction profiles for the R-phase of $Bi_{0.9}Nd_{0.1}FeO_3$ at room temperature (Table 1). (c, d) Experimental (crosses) and calculated (line) profiles for the O_1 phase of $Bi_{0.9}Nd_{0.1}FeO_3$ at 873 K (Table 1). The upper (a, c) and lower plots (b, d) plots for each temperature represent the $2\theta = 35°$ and $2\theta = 154°$ detector banks. The four-bank R_{wp} values were 3.69% and 3.33% for the data at 298 and 873 K, respectively.

dx.doi.org/10.1021/cm1036925 |Chem. Mater. 2011, 23, 2166–2175

Table 1. Structural (nuclear) Parameters for the *R* and O_1 Phases of $Bi_{0.9}Nd_{0.1}FeO_3$ Obtained by Rietveld Refinements Using Neutron Powder Diffraction Data Collected at 298 and 873 K, Respectively

atom	site	*x*	*y*	*z*	U_{iso}, ×100 (Å^2)
		R-Phase: Space Group *R*3*c* (No. 161), *a* = 5.56819(3) Å, *c* = 13.7856(1) Å			
$Bi_{0.9}Nd_{0.1}$	6*a*	0	0	0.04393(6)	0.92(2)
Fe	6*a*	0	0	0.26752(6)	0.45(1)
O	18*b*	0.4434(1)	0.0177(1)	0	0.83[a]
		O_1-Phase: Space Group *Pbnm* (No. 62), *a* = 5.4387(7), *b* = 5.63331(8), *c* = 7.9101(1)			
$Bi_{0.9}Nd_{0.1}$	4*c*	−0.0044(3)	0.03634(2)	1/4	3.64[b]
Fe	4*b*	0	1/2	0	1.31(6)
O1	4*c*	0.0779(3)	0.4792(3)	1/4	2.85[c]
O2	8*d*	0.7045(2)	0.2926(2)	0.0389(2)	3.23[d]

[a] U_{11} = 0.89(3), U_{22} = 0.52(3), U_{33} = 1.04(3), U_{12} = 0.024(3), U_{13} = −0.10(2), U_{23} = 0.30(2). [b] U_{11} = 2.72(7), U_{22} = 3.51(8), U_{33} = 4.7(1), U_{12}= −0.08(7), U_{13} = U_{23} = 0. [c] U_{11} = 2.8(1), U_{22} = 4.3(1), U_{33} = 1.4(1), U_{12}= −0.57(8), U_{13}=U_{23} = 0. [d] U_{11} = 2.81(6), U_{22} = 2.42(6), U_{33} = 4.46(9), U_{12} = −2.13(7), U_{13} = 1.05(6), U_{23} = −1.25(6).

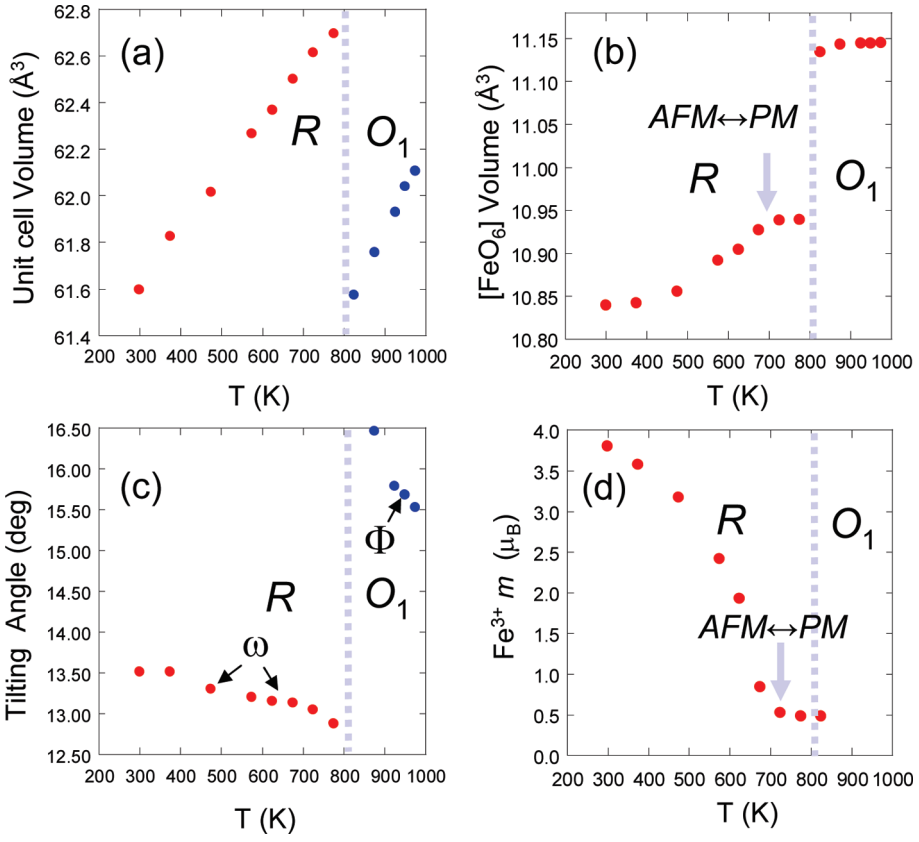

Figure 3. Temperature dependences of selected structural parameters in $Bi_{0.9}Nd_{0.1}FeO_3$ obtained from refinements using neutron powder diffraction data: (a) unit cell volume, (b) [FeO_6] volume, (c) tilting angle, and (d) Fe^{3+} magnetic moment. Note the opposite behavior of the unit cell and [FeO_6] volumes across the $R \leftrightarrow O_1$ transition.

the $O_2 \leftrightarrow O_1$ transition, results in extremely fragile sintered pellets which are difficult to handle.

X-ray diffraction (XRD) patterns were collected using a Panalytical (note that the use of brand or trade names does not imply endorsement of the product by NIST) X′Pert Pro diffractometer equipped with a Ge single-crystal incident beam monochromator (Cu $K\alpha_1$ radiation), a Pixcel position sensitive detector, and Anton Paar HTK-450 and XRK-16 stages. A Philips CM30 TEM operated at 200 kV and equipped with a double-tilt high-temperature stage was used for electron diffraction and imaging. An FEI Titan TEM operated at 300 kV was used for high-resolution structural imaging. Neutron powder diffraction data were collected for the *x* = 0.1 and *x* = 0.175 samples using the BT-1 (wavelength 1.5402(2) Å) and GEM (time-of-flight) instruments located at NIST and ISIS (Rutherford Appleton Laboratory), respectively. In both cases, the sample powders were loaded in thin-walled vanadium containers. Variable-temperature measurements were performed using a closed-cycle refrigerator (BT-1) and a high-temperature furnace (GEM). Rietveld refinements were performed using the GSAS

dx.doi.org/10.1021/cm1036925 |*Chem. Mater.* 2011, 23, 2166–2175

software package.[16] SARAh software[17] was combined with GSAS for symmetry-constrained magnetic-structure refinements. The refinements using GEM data included the diffraction patterns collected in four detector banks (centered at $2\theta \approx 35°$, 63°, 91°, and 154°).

Variable field (from +5570 kA/m = 70 000 Oe to −5570 kA/m) and temperature (from 300 to 1000 K) magnetic measurements were performed on sintered pellets using a Quantum Design superconducting quantum interference device (SQUID) vibrating-sample magnetometer (VSM) equipped with a sample oven. Before each variable-temperature scan, the sample was first subjected to a strong magnetic field of 70 000 Oe, and the field was then reduced to a selected value. Low-temperature magnetic measurements (from 4 to 300 K) were performed in a conventional SQUID instrument.

RESULTS AND DISCUSSION

R ↔ O_1 Phase Transition. The neutron diffraction patterns for $Bi_{0.9}Nd_{0.1}FeO_3$ (Figure 2) can be fitted satisfactorily assuming the rhombohedral *R*3*c* (No. 161) and orthorhombic *Pbnm* (No. 62) structural models below and above 823 K, respectively. Below 723 K, magnetic reflections evolve due to the G-type AFM ordering of Fe^{3+} magnetic moments. The rhombohedral structure was refined assuming a model with the ions located at the following positions: Bi/Nd $(0, 0, z \approx 0 + s)$, Fe $(0, 0, z \approx 1/4 + t)$, and O $(x \approx 1/2, y \approx 0, z = 0)$, where parameters *s* and *t* reflect displacements of the Bi/Nd- and Fe-cations off their ideal positions, respectively. As in previous refinements of the $BiFeO_3$ structure,[18] the coordinate of oxygen positions was fixed at $z = 0$. The model assumed isotropic atomic displacement parameters (ADP) for Bi/Nd and Fe and anisotropic for O (refinements using anisotropic ADP for Bi/Nd converged but revealed no significant anisotropy). The high-temperature orthorhombic structure was refined in a nonstandard setting for space group No. 62, *Pbnm* with lattice parameters $\sqrt{2}a_c \times \sqrt{2}a_c \times 2a_c$ and atoms occupying the following positions: Bi/Nd $(x \approx 0, y \approx 0 + v, 1/4)$, Fe $(0, 1/2, 0)$, O1 $(x \approx 3/4, y \approx 1/4, z \approx 0)$, and O2 $(x \approx 0, y \approx 1/2, 1/4)$, where the parameter *v* describes the displacements of the Bi/Nd cations off the ideal positions (the nonstandard *Pbnm* setting was selected to facilitate comparison between the O_1 and O_2 structures). Anisotropic ADP values were refined for all sites.

Temperature dependencies of the principal structural characteristics are summarized in Figure 3. Similar to $BiFeO_3$,[6] the $R \leftrightarrow O_1$ transition is accompanied by abrupt expansion of the unit cell volume in the *R* phase by ≈1.8%. The magnitude of cation displacements off their ideal positions increases abruptly in the *R*-structure (not shown). The changes in the unit cell volume across the transition are manifested in the volumes of the cation sublattices, as inferred from the Bi−Bi and Fe−Fe distances. The unit cell volume *V* in perovskites is determined by the sum of $[AO_{12}]$ (V_A) and $[BO_6]$ (V_B) polyhedral volumes according to $V = Z(V_A + V_B)$, where *Z* is the number of perovskite formula in the unit cell. The octahedral V_B volume, calculated directly from the refined oxygen coordinates, contracts by ≈1.8% while the V_A volume, calculated as $V_A = V - V_B$, expands by ≈2.6% upon crossing into the *R* phase. The *R* and O_1 phases exhibit $a^-a^-a^-$ and $a^-a^-c^+$ types of octahedral tilting, respectively. As illustrated in Figure 4, the octahedra rotate about the 3-fold symmetry axis (angle ω) in the *R*-phase. In the O_1 phase, the octahedra rotate about both their twofold (*a*-axis, angle θ) and pseudo fourfold (*c*-axis, angle ϕ) symmetry axes. In the present case, the refinements indicate that $\cos(\theta) \approx [\cos(\phi)]^2$ so that the rotation axes for individual octahedra in the O_1 structure are close

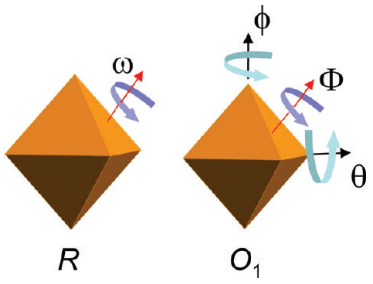

Figure 4. Schematic illustration of octahedral rotations in the *R* and O_1 structures.

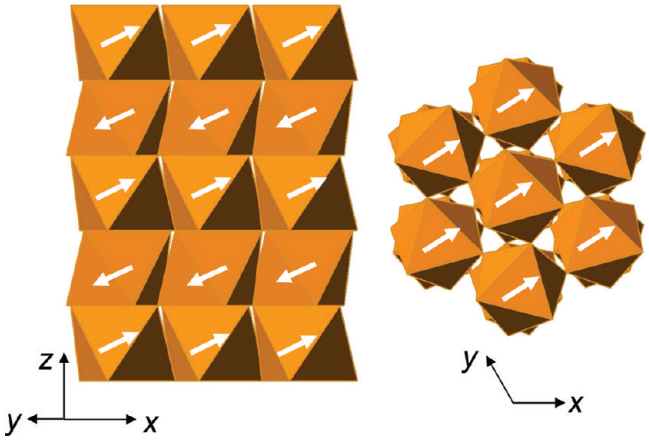

Figure 5. Schematic rendering of the refined *R*3*c* structure of $Bi_{0.9}Nd_{0.1}FeO_3$ with arrows indicating the directions of magnetic moments.

to the pseudo threefold axes. The angle Φ of these rotations, which can be directly compared to ω, is calculated according to $\cos(\Phi) = \cos(\theta)\cos(\phi)$. The results (Figure 3) indicate that an abrupt decrease in the tilting angle accompanies the $O_1 \rightarrow R$ transition, as expected for a simultaneous expansion of the cation sublattices and contraction of the octahedral volumes.

Refinements of the magnetic structure indicated preferential alignment of the Fe^{3+} magnetic dipoles along the $\langle 11\bar{2}0 \rangle$ directions in the *c*-planes (Figure 5). The magnetic dipoles are inclined to the *c*-plane by ≈25°; this angle remained approximately constant up to the Neel temperature (T_N). The temperature dependence of the refined value of the magnetic moment is illustrated in Figure 3d. Fitting the Brillouin function ($J = 5/2$) to these data yields $T_N \approx 690$ K and a ground-state magnetic moment $m_0 \approx 4.15\ \mu_B$; these numbers are rather approximate considering the relatively limited temperature range of the measurements. The T_N value is somewhat higher compared to $BiFeO_3$ ($T_N \approx 650$ K) but agrees well with the variable-temperature magnetic measurements reported for $Bi_{0.9}Nd_{0.1}FeO_3$.[15]

O_2 Structure and $O_2 \leftrightarrow O_1$ Phase Transition. Detailed analysis of the $O_2 \leftrightarrow O_1$ transition was performed for the composition $Bi_{0.825}Nd_{0.175}FeO_3$. The X-ray and neutron diffraction patterns of the O_2 phase can be readily accounted for by a $PbZrO_3$-type *Pbam* (No. 55) structure with lattice parameters $\sqrt{2}a_c \times 2\sqrt{2}a_c \times 2a_c$. The principal features of this structure are (i) antipolar displacements of Bi parallel to the *a*-axis which double the periodicity along the *b*-axis and (ii) $a^-a^-c^0$ octahedral tilting; the structure exhibits severe distortions of the oxygen octahedra. Rietveld refinements using the *Pbam* model yield

dx.doi.org/10.1021/cm1036925 |*Chem. Mater.* 2011, 23, 2166–2175

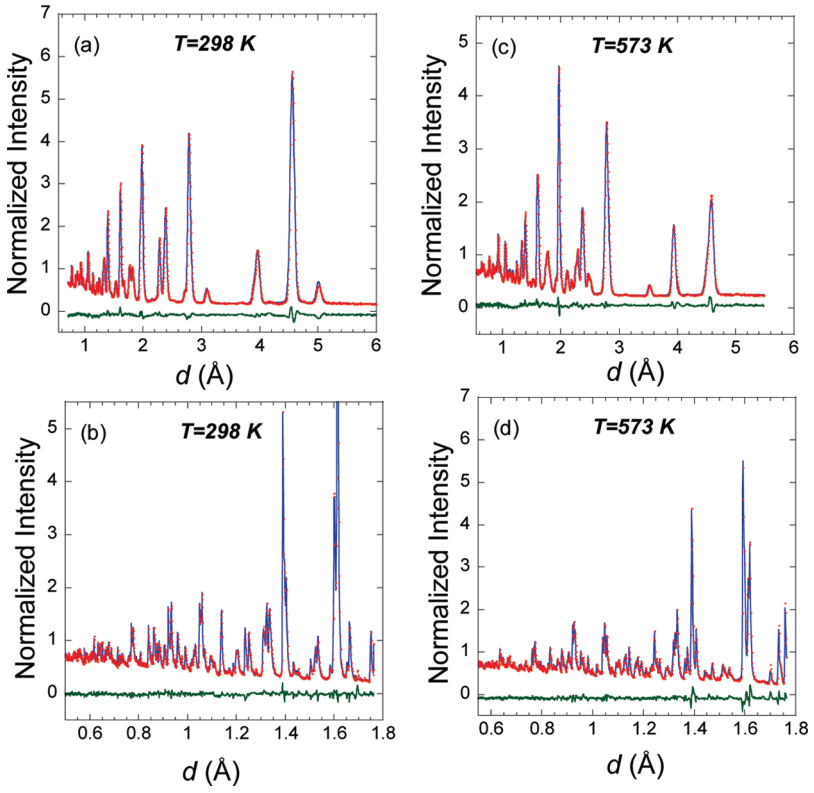

Figure 6. (a, b) Experimental (crosses) and calculated (line) neutron powder diffraction profiles for the O_2 phase of $Bi_{0.825}Nd_{0.175}FeO_3$ at room temperature (Table 2). (c, d) Experimental (crosses) and calculated (line) profiles for the O_1 phase of $Bi_{0.825}Nd_{0.175}FeO_3$ at T = 573 K (Table 2). The upper (a, c) and lower plots (b, d) plots for each temperature represent the 35° and 154° detector banks. The four-bank R_{wp} values were 3.37% and 4.68% for the data at 298 and 573 K, respectively.

Table 2. Structural (nuclear) Parameters for the O_2 and O_1 Phases of $Bi_{0.825}Nd_{0.175}FeO_3$ Obtained by Rietveld Refinements Using Neutron Powder Diffraction Data Collected at 298 and 648 K, Respectively

atom	site	x	y	z	U_{iso}, ×100 (Å^2)
		O_2-Phase: Space Group *Pbam* (No. 55), a = 5.58663(6) Å, b = 11.2235(1) Å, c = 7.79956(6) Å			
$Bi_{0.825}Nd_{0.175}$	4	0.7970(6)	0.1320(3)	0	1.22[a]
$Bi_{0.825}Nd_{0.175}$	4	0 0.7934(6)	0.1266(3)	0.2517(3)	2.14[b]
Fe	8	0.2582(2)	0.1215(2)	0.2517(3)	0.34(1)
O1	4	0.1964(6)	0.0883(4)	0	1.05[c]
O2	4	0.7215(7)	0.3379(4)	1/2	2.25[d]
O3	8	−0.0409(4)	0.2381(2)	0.2128(4)	1.84[e]
O4	4	0	1/2	0.2779(6)	3.88[f]
O5	4	0	0	0.3055(4)	1.66[g]
		O_1-Phase: Space group *Pbnm* (No. 62), a = 5.4387(7), b = 5.63331(8), c = 7.9101(1)			
$Bi_{0.825}Nd_{0.175}$	4*c*	−0.0058(2)	0.0428(1)	1/4	2.19[h]
Fe	4*b*	0	1/2	0	0.78(1)
O1	4*c*	0.0835(2)	0.4765(2)	1/4	1.63[i]
O2	8*d*	0.7013(1)	0.2957(1)	0.0417(1)	2.06[j]

[a] U_{11} = 2.1(1), U_{22} = 0.9(2), U_{33} = 0.7(1), U_{12} = −0.6(1), U_{13} = U_{23} = 0. [b] U_{11} = 1.9(2), U_{22} = 1.94(2), U_{33} = 2.6(2), U_{12} = 0.79(1), U_{13} = U_{23} = 0. [c] U_{11} = 0.6(1), U_{22} = 1.4(2), U_{33} = 1.1(1), U_{12} = 0.2(1), U_{13} = U_{23} = 0. [d] U_{11} = 3.94(6), U_{22} = 0.5(1), U_{33} = 2.2 (1), U_{12} = 0.5(2), U_{13} = U_{23} = 0. [e] U_{11} = 1.7(1), U_{22} = 2.3(1), U_{33} = 1.4 (1), U_{12} = 1.3(1), U_{13} = −1.5(1), U_{23} = −1.8(1). [f] U_{11} = 3.4(2), U_{22} = 4.9(3), U_{33} = 3.3 (3), U_{12} = −4.5(2), U_{13} = U_{23} = 0. [g] U_{11} = 2.2(2), U_{22} = 2.0(2), U_{33} = 0.8 (1), U_{12} = −1.9(1), U_{13} = U_{23} = 0. [h] U_{11} = 1.86(4), U_{22} = 1.80(4), U_{33} = 2.92(5), U_{12} = 0.24(5), U_{13} = U_{23} = 0. [i] U_{11} = 1.82(6), U_{22} = 2.32(7), U_{33} = 0.76(7), U_{12} = −0.57(8), U_{13} = U_{23} = 0. [j] U_{11} = 1.77(4), U_{22} = 1.53(4), U_{33} = 2.87(6), U_{12} = −1.25(4), U_{13} = 0.77(4), U_{23} = −0.92(4)

acceptable fits (Figure 6) but also large and strongly anisotropic ADP values for the Bi/Nd and O sites, as illustrated in Figure 7, suggesting that the actual structure deviates from the assumed atomic arrangement. Refinements of the magnetic structure with

dx.doi.org/10.1021/cm1036925 |*Chem. Mater.* 2011, 23, 2166–2175

a G-type AFM model demonstrated preferential alignment of the Fe^{3+} magnetic dipoles with the orthorhombic *c*-axis.

Deviations from the *Pbam* $\sqrt{2}a_c \times 2\sqrt{2}a_c \times 2a_c$ model, highlighted by large anisotropic ADP values, are consistent with the previously reported electron diffraction data[12] which revealed a series of $^1/_4 00l_c$-type superlattice reflections indicating additional doubling of the perovskite supercell to $\sqrt{2}a_c \times 2\sqrt{2}a_c \times 4a_c$. Reflection conditions in the selected area electron diffraction patterns (Figure 8) identify the space group for this $\sqrt{2}a_c \times 2\sqrt{2}a_c \times 4a_c$ superstructure as *Pbnm* (No. 62). High-temperature electron diffraction experiments (Figure 9) performed in the $\langle 130 \rangle_c$ orientation that enables simultaneous observation of the $^1/_4 hh0_c$- ($PbZrO_3$-like) (indicated using red arrows in Figure 9) and $^1/_4 00l_c$-type superlattice reflections (indicated using black arrows) demonstrate that the $^1/_4 hh0_c$ reflections appear at the $O_2 \leftrightarrow O_1$ transition, whereas the $^1/_4 00l$-type reflections emerge

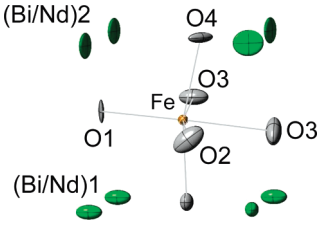

Figure 7. Schematic rendering of the refined O_2 structure of $Bi_{0.825}Nd_{0.175}FeO_3$. Note large values and strong anisotropy for the Bi/Nd and oxygen atomic displacement parameters.

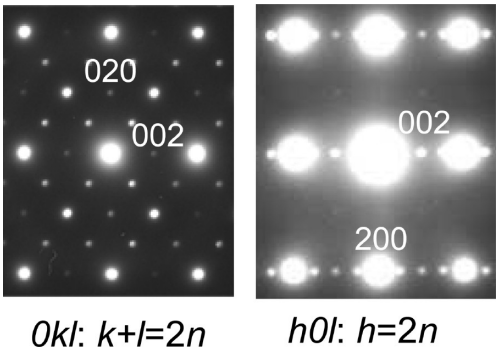

Figure 8. Representative electron diffraction patterns recorded from a single grain of the O_2 phase of $Bi_{0.825}Nd_{0.175}FeO_3$ at room temperature. The reflection conditions match the *Pbnm* space group.

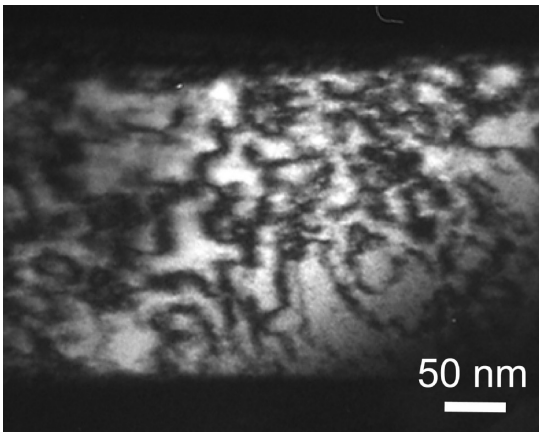

Figure 10. Dark-field image recorded with a $^1/_4 hh0_c$-type reflection strongly excited near the $[103]_c$ orientation reveals antiphase domains associated with Bi displacements. The dark lines in the image correspond to the antiphase boundaries.

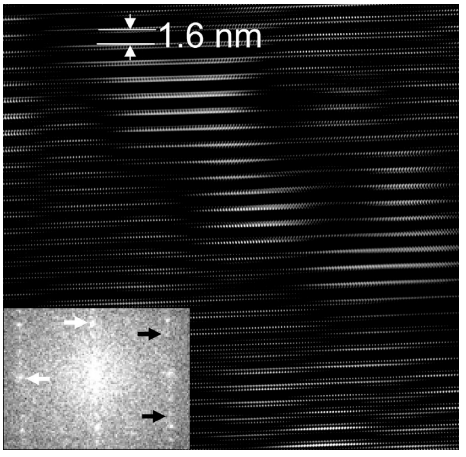

Figure 11. Fourier-filtered image of $Bi_{0.85}Nd_{0.15}FeO_3$ in $\langle 110 \rangle_c$ orientation obtained using a combination of $^1/_4 00l_c$-type (indicated using black arrows, weight 150%) and fundamental (indicated using white arrows, weight 10%) frequencies in the Fourier transform (inset) from the raw experimental high-resolution TEM image. This image reveals that domains of the *Pbnm* superstructure are confined to the nanoscale. Antiphase shifts along the *c*-axis between the neighboring domains are clearly observed.

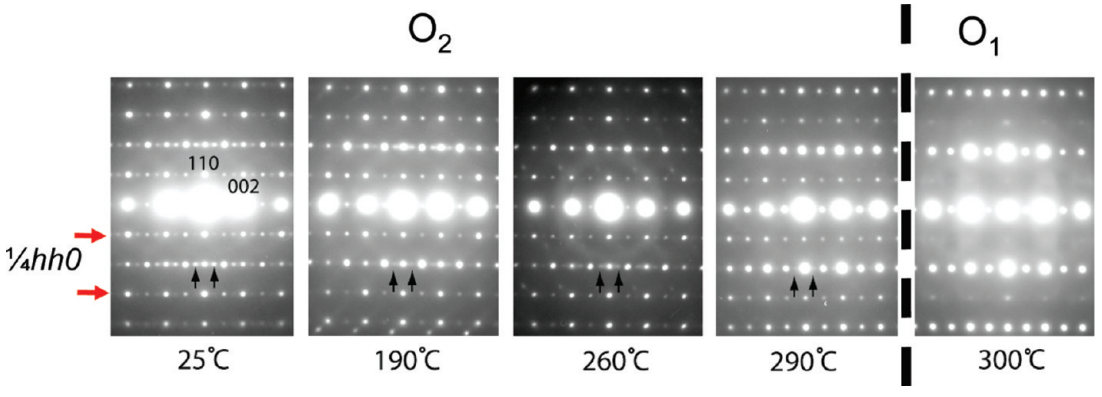

Figure 9. Variable-temperature electron diffraction data for $Bi_{0.85}Nd_{0.15}FeO_3$ recorded from the single grain in $[103]_c$ orientation. This orientation contains both $^1/_4 hh0_c$ and $^1/_4 00l_c$ reflections. The data suggests that $^1/_4 00l_c$ reflections evolve at temperatures lower than that of the $O_2 \leftrightarrow O_1$ transition.

dx.doi.org/10.1021/cm1036925 |*Chem. Mater.* 2011, 23, 2166–2175

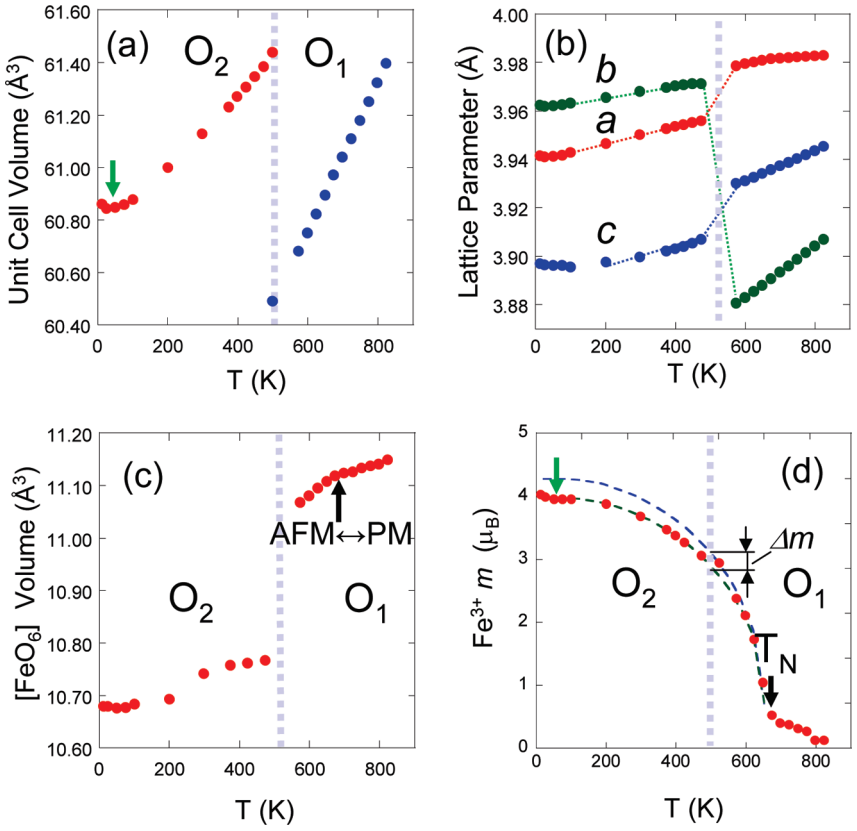

Figure 12. Temperature dependences of selected structural parameters in $Bi_{0.825}Nd_{0.175}FeO_3$ obtained from refinements using neutron powder diffraction data: (a) unit cell volume, (b) lattice parameters, (c) [FeO_6] volume, and (d) Fe^{3+} magnetic moment. The behavior of the unit cell and [FeO_6] volumes is similar to that observed for the $R \leftrightarrow O_1$ transition in Figure 3. The green arrow indicates the low-temperature magnetic-dipole-reorientation transition. Dashed lines in (d) represent fits of the Brillouin function to the m(T) data above (green) and below (blue) the structural transition.

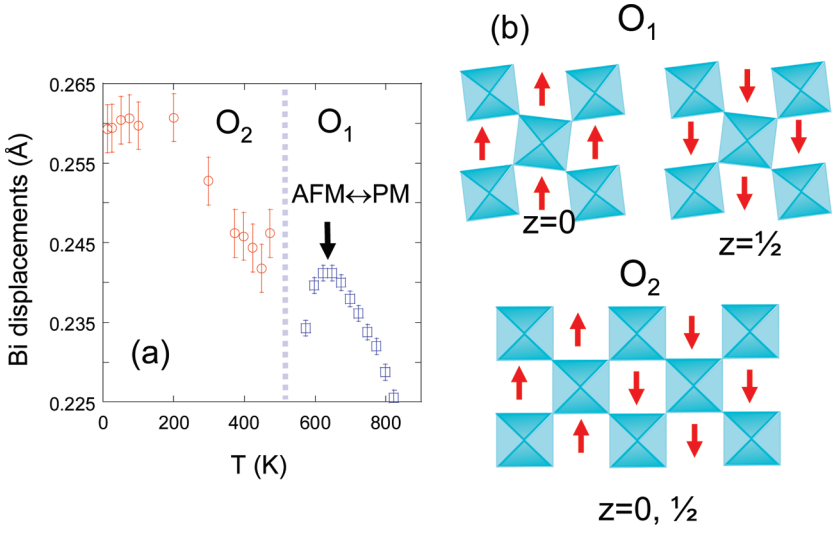

Figure 13. (a) Temperature dependence of the magnitude of Bi displacements off the ideal fixed coordinate positions. (b) Schematic illustration of Bi displacement patterns (arrows) in the O_1 and O_2 structures.

at a lower temperature. Dark-field imaging (room-temperature) using $^1/_4hh0_c$-type reflections revealed antiphase domains (Figure 10) that feature out-of-phase Bi displacements, whereas images recorded with $^1/_400l_c$ produced only a faint speckled contrast (not shown). High-resolution TEM imaging (Figure 11) confirmed that the superstructure giving rise to the $^1/_400l_c$-type reflections is limited to the nanoscale, which explains why these reflections remain indistinct in X-ray and neutron powder diffraction patterns.

dx.doi.org/10.1021/cm1036925 |*Chem. Mater.* 2011, 23, 2166–2175

The plausible models for the quadrupled (i.e., $4a_c$) periodicity in the $\sqrt{2}a_c \times 2\sqrt{2}a_c \times 4a_c$ superstructure include (1) $NaNbO_3$-like octahedral tilting[19] with a sequence of two octahedra rotating about the *c*-axis in one direction, followed by two octahedra rotating in the opposite direction, and (2) a $BiScO_3$-like[20] sequence of Bi *c*-layers featuring antipolar ($PbZrO_3$-like) Bi displacements within each layer, with displacements in the successive *c*-layers occurring out of phase. A combination of $NaNbO_3$-like tilting and antipolar Bi displacements readily yields the required *Pbnm* symmetry, whereas none of the possible $BiScO_3$-like sequences of the displaced Bi planes appears to conform to this space group. As noted in ref 15, $NaNbO_3$-like tilting $a^-a^-c^+/a^-a^-c^-$ is probable because it is intermediate between the tilting systems $a^-a^-a^-$ and $a^-a^-c^+$ in the

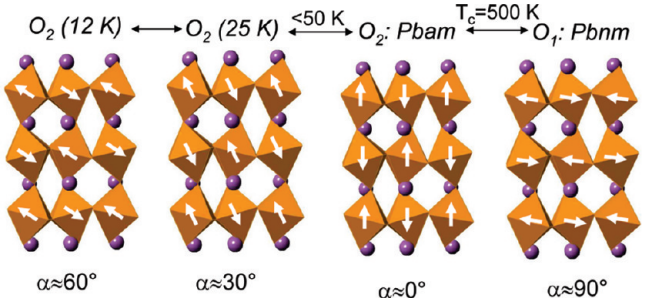

Figure 14. Schematic rendering of the orientations of magnetic moments in $Bi_{0.825}Nd_{0.175}FeO_3$ as a function of temperature. Here, α denotes the angle between the direction of the magnetic moment and the *c*-axis. Note the two dipole reorientation transitions: one at the $O_2 \leftrightarrow O_1$ structural transition and another below 50 K.

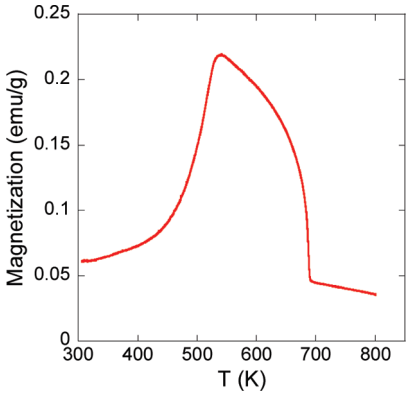

Figure 16. Temperature dependence of magnetization for the zero-field-cooled $x = 0.175$ sample under $H = 1000$ Oe.

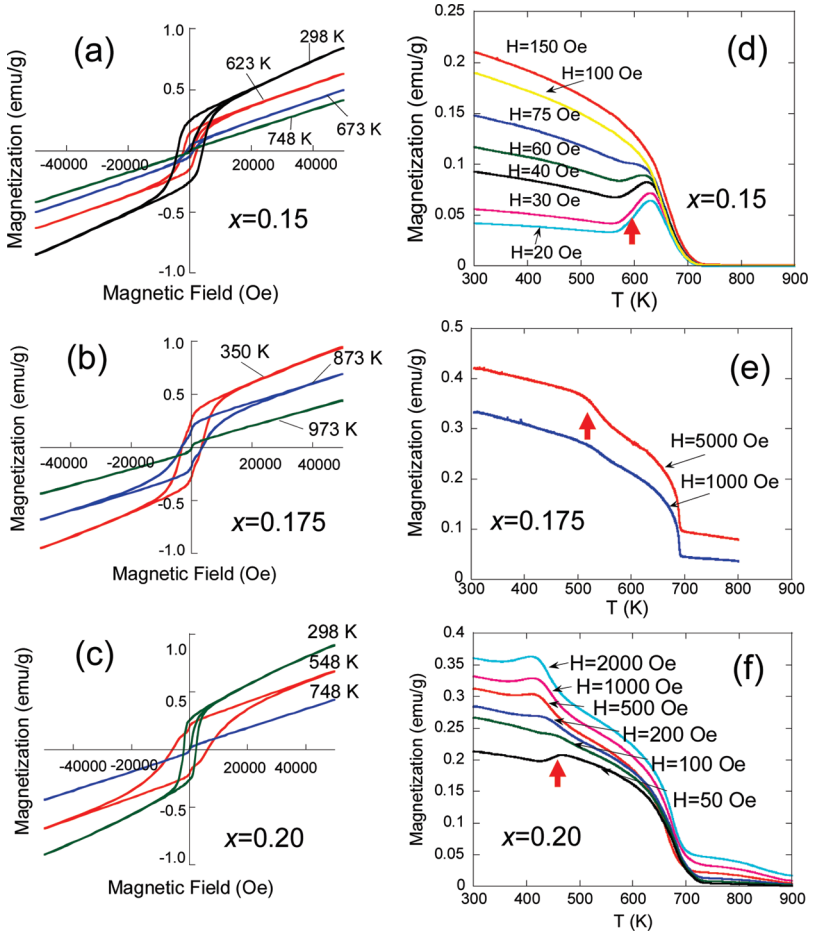

Figure 15. Magnetic hysteresis loops at selected temperatures for $x = 0.15$ (a), 0.175 (b), and 0.20 (c). Temperature dependence of magnetization, $M(T)$, for the same compositions: (d) $x = 0.15$, (e) $x = 0.175$, and (f) $x = 0.20$. A magnetization anomaly near the $O_2 \leftrightarrow O_1$ transition is indicated using an arrow. Note that the temperature of this anomaly decreases systematically with increasing Nd content as does the temperature of the $O_2 \leftrightarrow O_1$ transition. Prior to each $M(T)$ measurement the samples were cooled from high temperature under a field $H = 70000$ Oe. Then, the desired magnetic field was applied and the $M(T)$ dependence was measured on heating.

dx.doi.org/10.1021/cm1036925 |*Chem. Mater.* 2011, 23, 2166–2175

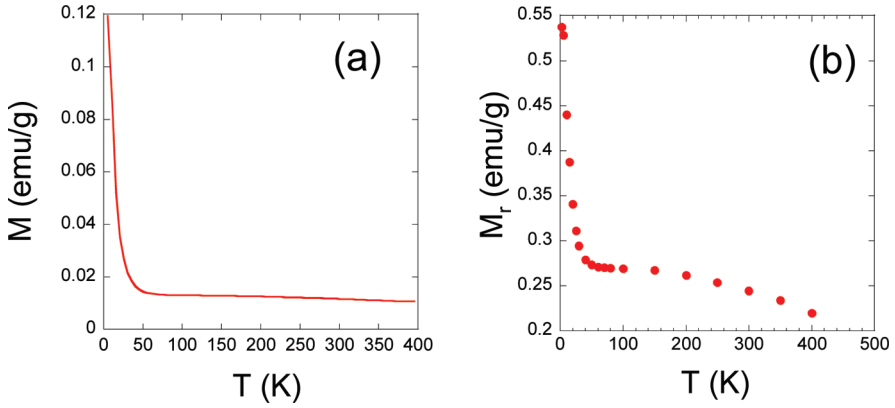

Figure 17. (a) Temperature dependence of magnetization (cooled under $H = 75$ Oe) below room temperature for $Bi_{0.85}Nd_{0.15}FeO_3$. (b) Temperature dependence of the remnant magnetization for the same composition as extracted from $M(H)$ hysteresis loops. The anomaly below 50 K was attributed to reorientation of the dipoles as identified using neutron diffraction.

end-compounds $BiFeO_3$ and $NdFeO_3$, respectively. However, Rietveld refinements using a model based on the $NaNbO_3$-like tilting and isotropic ADP values for all atoms were inconclusive as they produced a quality of fit comparable to that for the *Pbam* model with isotropic ADPs. Refinements of anisotropic ADPs for the $a_c \times 2\sqrt{a_c} \times 4a_c$ model were not practical due to a large number of structural variables. Structural refinements using total neutron scattering data (real and reciprocal space) to identify the origin of the quadrupled *c*-axis periodicity are in progress and, if successful, will be reported elsewhere.

In the present study, we used the *Pbam* model to analyze the temperature dependence of the structural parameters for the O_2 phase. The $O_2 \leftrightarrow O_1$ transition for $Bi_{0.825}Nd_{0.175}FeO_3$ occurs around T = 500 K and bears clear similarities to the $R \leftrightarrow O_1$ transition, as manifested in an abrupt expansion of the unit cell volume with concurrent contraction of the octahedral volume in the O_2 phase (Figure 12a). These volume changes are accompanied by disappearance of the *in-phase* tilting in the O_2 structure. Calculations of the tilting angle about the *b*-axis in the O_2 structure are limited by the octahedral distortions. The expansion of the unit cell volume in the O_2 phase below the $O_1 \rightarrow O_2$ transition is determined by the lattice parameter *b* (Figure 12b) which corresponds to the direction orthogonal to Bi displacements in both the O_1 and the O_2 structures. The temperature dependence of the refined Bi displacements relative to the ideal fixed coordinate positions is displayed in Figure 13a. Bi displacements in both the O_1 and O_2 structures occur along the twofold symmetry axes parallel to the rotation axes of the [FeO_6] octahedra (a^-a^- tilt); however, the displacement patterns in the two structures are different (Figure 13b). The magnitude of Bi displacements in the O_1 structure exhibits an apparent anomaly at the temperature of the magnetic transition which suggests strong coupling of Bi displacements (and octahedral tilting) to the magnetic ordering. Another discontinuous change occurs at the $O_1 \leftrightarrow O_2$ transition.

As reported previously,[15] the $O_1 \rightarrow O_2$ transition is accompanied by an abrupt *a*- to *c*-axis reorientation of magnetic dipoles. The intensity distribution among the 141/221 and 023 magnetic reflections is very sensitive to orientations of magnetic moments and enables reliable identification of the moment directions.[14] Below 50 K, a *reverse c*- to *a*-axis reorientation of the magnetic moments is observed (Figure 14); however, in this case, the reorientation transition is gradual without any detectable

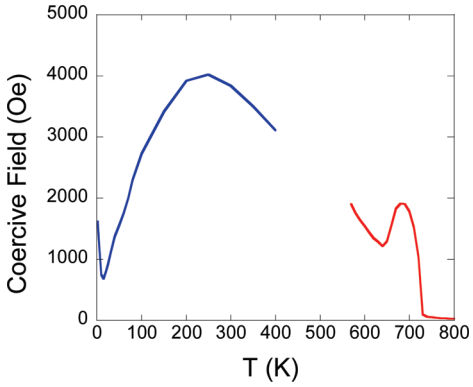

Figure 18. Temperature dependence of the coercive field for $Bi_{0.85}Nd_{0.15}FeO_3$. The high- and low-temperature portions of this curve were obtained in separate experiments using two different instruments (SQUID-VSM for high temperatures and SQUID for low temperatures), as indicated using different colors.

changes in the nuclear structure. The temperature dependence of the refined Fe^{3+} magnetic moment exhibits anomalies at both the $O_1 \leftrightarrow O_2$ and low-temperature dipole-reorientation transitions (Figure 12d); in particular, the magnetic moment is reduced abruptly at the $O_1 \leftrightarrow O_2$ transition. Fitting the Brillouin function to the data below the structural transition returns $T_N \approx 673$ K and a ground-state moment $m_0 \approx 4.05\ \mu_B$ whereas a similar fit to the data above the transition yields $m_0 \approx 4.4\ \mu_B$.

Structural $O_1 \leftrightarrow O_2$ Transition and Magnetic Response. The *R*-phase of $Bi_{0.9}Nd_{0.1}FeO_3$ exhibits very narrow magnetic hysteresis loops,[15] whereas for higher concentrations of Nd, a robust ferromagnetic response occurs below the magnetic transition. Figure 15 summarizes the magnetic hysteresis loops, M(H), and the temperature dependence of magnetization, M(T), between room temperature and 900 K for three $Bi_{1-x}Nd_xFeO_3$-compositions (x = 0.15, 0.175, and 0.20) within the O_2 phase field. In addition to a steep rise in magnetization at the magnetic transition, a second anomaly is observed which presumably arises due to the $O_2 \leftrightarrow O_1$ phase transition;[14] the exact temperature of this magnetic anomaly is field dependent. An example of the $M(T)$ dependence for a zero-field-cooled sample (x = 0.175) is shown in Figure 16. The change in magnetization at the $O_2 \leftrightarrow O_1$

dx.doi.org/10.1021/cm1036925 |*Chem. Mater.* 2011, 23, 2166–2175

transition correlates with a decrease of the Fe^{3+} magnetic moment (Figure 12).

The second dipole-reorientation transition below 50 K, which occurs without any detectable structural transition, is also manifested in a magnetization anomaly (Figure 17); however, this change in magnetization is not abrupt, which is consistent with the results inferred from neutron diffraction. Interestingly, the coercive field exhibits well-defined anomalies at both the $O_2 \leftrightarrow O_1$ transition and the low-temperature magnetic-dipole-reorientation transition (Figure 18). Overall, the present results indicate a very intimate coupling between the displacive (tilting, cation displacements) and magnetic order parameters which is manifested in their well-defined anomalies at the temperatures of the magnetic and structural phase transitions.

CONCLUSIONS

Rietveld refinements using neutron powder diffraction data revealed some similarities between the $R \leftrightarrow O_1$ and $O_2 \leftrightarrow O_1$ phase transitions in Nd-substituted $BiFeO_3$. In particular, both structural transitions are accompanied by a large discontinuous expansion of the lattice volume with concurrent contraction and expansion of the $[FeO_6]$ and $[(Bi/Nd)O_{12}]$ polyhedral volumes, respectively, in the low-temperature polymorphs (i.e., R and O_2). The octahedral tilting angle decreases abruptly in the low-temperature polymorphs. The expanded $[(Bi/Nd)O_{12}]$ volumes and reduced octahedral tilting angles correlate with a stronger off-centering of the A-cations in the R and O_2 structures compared to the O_1 phase. The $O_2 \leftrightarrow O_1$ transition, which occurs in the magnetically ordered state, is also accompanied by abrupt 90° reorientation of magnetic dipoles from an a-axis orientation in the O_1 $Pbnm$ structure to a c-axis orientation in the O_2 $Pbam$ phase. The magnetic moments retain their overall G-type antiferromagnetic arrangement. The magnetic dipoles in the O_2 structure undergo an additional reorientation transition below 50 K by rotating back to the orientation corresponding to the high-temperature O_1 structure. This low-temperature reorientation, which occurs without qualitative changes in the nuclear structure, is gradual and still remains incomplete at 10 K. The structural parameters of the R and O_2 structures exhibit discernible anomalies at the temperature of the magnetic transition. Concurrently, the structural $O_2 \leftrightarrow O_1$ transition is accompanied by abrupt changes in magnetization and coercive field.

Recent studies[21] of thin films in the related $(Bi,Sm)FeO_3$ system indicated that a transition from the paraelectric O_1 structure to a ferroelectric (FE) phase can be induced at room-temperature by applying an electric field to films with compositions in the O_1 phase field near the $O_1 \leftrightarrow O_2$ phase boundary. Our present results suggest that this electric-field-induced $O_1 \leftrightarrow$ FE transition should also generate a large volume change and a significant effect on magnetization, thereby enabling room-temperature electromagnetic coupling in a single-phase material.

REFERENCES

(1) Catalan, G.; Scott, J. F. *Adv. Mater.* **2009**, *21*, 2463.
(2) Ramesh, R.; Spaldin, N. A. *Nat. Mater.* **2007**, *6*, 21.
(3) Glazer, A. M. *Acta Crystallogr.* **1972**, *B28*, 3384.
(4) Moreau, J. M.; Michel, C.; Gerson, R.; James, W. J. *J. Phys. Chem. Solids* **1971**, *32*, 1315.
(5) Kubel, F.; Schmid, H. *Acta Crystallogr.* **1990**, *B46*, 698.
(6) Arnold, D. C.; Knight, K. S.; Morrison, F. D.; Lightfoot, P. *Phys. Rev. Lett.* **2009**, *102*, 027602.
(7) Sosnowska, I.; Pterlin-Neumaier, T.; Steichele, E. *J. Phys. C* **1982**, *15*, 4835.
(8) Yuan, G. L.; Or, S. W.; Liu, J. M.; Liu, Z. G. *Appl. Phys. Lett.* **2006**, *89*, 052905.
(9) Khomchenko, V. A.; Shvartsman, V. V.; Borisov, P.; Kleemann, W.; Kiselev, D. A.; Bdikin, I. K.; Vieira, J. M.; Kholkin, A. L. *Acta Mater.* **2009**, *57*, 5137.
(10) Nalwa, K. S.; Garg, A. *J. Appl. Phys.* **2008**, *103*, 044101.
(11) Karimi, S.; Reaney, I. M.; Han, Y.; Pokorny, J.; Sterianou, I. *J. Mater. Sci.* **2009**, *44*, 5102.
(12) Karimi, S.; Reaney, I. M.; Levin, I.; Sterianou, I. *Appl. Phys. Lett.* **2009**, *94*, 112903.
(13) Cheng, C. J.; Kan, D.; Lim, S. H.; McKenzie, W. R.; Munroe, P. R.; Salamanca-Riba, L. G.; Withers, R. L.; Takeuchi, I.; Nagarajan, V. *Phys. Rev. B* **2009**, *80*, 014109.
(14) Rusakov, D.; Abakumov, A. M.; Yamaura, K.; Belik, A. A.; Van Tendeloo, G.; Takayama-Muromachi, E. *Chem. Mater.* **2010**, *23*, 285–292.
(15) Levin, I.; Karimi, S.; Provenzano, V.; Dennis, C. L.; Wu, H.; Comyn, T. P.; Stevenson, T. J.; Smith, R. I.; Reaney, I. M. *Phys. Rev.* **2010**, *B81*, 020103.
(16) Larson, A. C.; Von Dreele, R. B. Los Alamos National Laboratory LAUR Report No. 86-748; Los Alamos National Laboratory: Los Alamos, NM, 1994
(17) Wills, A. S. *Physica B* **2000**, *276*, 680.
(18) Selbach, S. M.; Tybell, T.; Einarsrud, M.-A.; Grande, T. *Adv. Mater.* **2008**, *20*, 3692.
(19) Hewatt, A. W. *Acta Crystallogr., Sect. B* **1982**, *24*, 1968.
(20) Trolier-McKinstry, S.; Biegalski, M. D.; Wang, J. L.; Belik, A. A.; Takayama-Muromachi, E.; Levin, I. *J. Appl. Phys.* **2008**, *104* (4), 044102.
(21) Kan, D.; Palova, L.; Anbusathaiah, V.; Cheng, C. J.; Fujino, S.; Nagarajan, V.; Rabe, K. M.; Takeuchi, I. *Adv. Funct. Mater.* **2010**, *20* (7), 1108–1115.